Journal of Power Sources 183 (2008) 214–225

Contents lists available at ScienceDirect

Journal of Power Sources

journal homepage: www.elsevier.com/locate/jpowsour

The effects of the interconnect rib contact resistance on the performance of planar solid oxide fuel cell stack and the rib design optimization

Shixue Liu, Ce Song, Zijing Lin*

Hefei National Laboratory for Physical Sciences at the Microscale and Department of Physics, University of Science and Technology of China, Hefei, Anhui 230026, China

ARTICLE INFO

Article history:
Received 5 March 2008
Received in revised form 20 April 2008
Accepted 21 April 2008
Available online 2 May 2008

Keywords:
Solid oxide fuel cell
Interconnect rib
Contact resistance
Concentration polarization
Cathode thickness
Design optimization

ABSTRACT

A mathematical model for the performance of the planar solid oxide fuel cell (SOFC) stack is described. The model considered the electric contact resistance between the electrode and interconnect rib, the gas transport in the electrodes, electronic and ionic conductions in the membrane-electrode assembly and the electrochemical reactions at the gas–electrode–electrolyte three phase boundaries. The model is capable of describing in detail the rib effect on the gas transport and the current distribution in the fuel cell. The contact resistance is found to be an important factor in limiting the SOFC performance. Based on the interplay of the concentration and ohmic polarizations, numerical results are provided for the optimal rib widths for different pitch sizes and different area specific contact resistance ($ASR_{contact}$). The optimal rib width is found to be linear to the pitch width for a given $ASR_{contact}$ and the parameters for the linearity are given. The parameters are little affected by the hydrogen concentration and the thickness, porosity or conductivity of the cathode. The influence of the cathode thickness on the SOFC performance is also examined. Contrary to the common belief on the thin cathode (~50 μm), thicker cathode layer (100–300 μm) is beneficial to the SOFC stack performance.

1. Introduction

Solid oxide fuel cell (SOFC) offers great potential for high efficiency, environmentally benign electric energy generation by converting chemical energy to electricity directly without passing through the combustion process and Carnot circle. There is a great deal of research on solid oxide fuel cells generally, especially on new material systems and on the optimizations of the microstructures to improve the electrochemical performance of the cell, or membrane-electrode assembly (MEA). Planar-type designs have received much attention because they potentially offer higher power density relative to the tubular-type SOFC, which is ascribed to the low electrical resistance due to shorter current paths. In particular, a very thin electrolyte film can be used in an anode-supported SOFC, drastically reducing the ohmic resistance and enabling operation at intermediate temperature [1–3]. However, relatively little of the literature concentrates on such critical technical issues as the system-level layout of the layers and stacks [4–6].

The most popular and reliable MEA materials for SOFCs comprise Y_2O_3-stabilized zirconia (YSZ) as the electrolyte and a constituent in the composite anode and cathode, Ni for the anode, and Sr-doped $LaMnO_3$ (LSM) for the cathode. Under ideal conditions with pure hydrogen fuel and low fuel utilization, numerous groups have reported over the years that single cells with optimized materials can yield power densities on the order of 1 W cm^{-2} or higher at the operating temperature of 700–800 °C [2,3,7–12]. For practical applications, however, multiple cells must be connected in series by interconnect material to form a fuel cell stack. The recently reported best performance of SOFC stacks with metallic bipolar plate current collectors [13,14] is substantially below that for the single cell [2,3]. The lowered cell performance in the stack may be attributed to the reduced gas transport and the increased ohmic polarization in the stack setting. When assembling the SOFC stack, the connecting materials (bipolar plates) are required. Small channels, which are often formed in the interconnect material, are commonly used to carry the fuel and air gas flow. The "ribs", which separate and define the flow channels, make direct contact with the electrodes. For technical reason, the channels and the ribs cannot be too small [15] and the contact resistance between the ribs and the electrodes is part of the intrinsic property of the interconnect material [16]. In designing the layer architecture, there is a tradeoff that must be considered between the rib and channel sizes. On one hand, wider ribs and ribs covering bigger fraction of the cell area may reduce the interface resistance to current flow by increasing the electrode–interconnect contact area and reducing the current path through the possibly high resistance electrode material. Hence,

* Corresponding author. Tel.: +86 551 3606345; fax: +86 551 3606348.
E-mail address: zjlin@ustc.edu.cn (Z. Lin).

0378-7753/$ – see front matter © 2008 Elsevier B.V. All rights reserved.
doi:10.1016/j.jpowsour.2008.04.054

such ribs will give a better conduction of the electrical current and reduce ohmic losses. On the other hand, the chemical species do not diffuse as well underneath wide ribs. Narrow ribs are needed to facilitate more uniform distribution of reactive gases across the area of the electrolyte surface and thus to promote electrochemical performance. The implication of the tradeoff to the cell performance can be very significant and a designer must decide how to configure a channel network to optimize the cell performance.

There have been a few pioneering works on the rib design optimization. Ferguson et al. [17] gave a numerical example for the rib size effect on the performance of a specific electrolyte-supported SOFC. Lin et al. [18] provided a phenomenological model and analytical expressions to estimate the rib effects on the concentration and ohmic polarizations of anode-supported SOFC stacks. Ji et al. [19] showed that the terminal output of a SOFC stack depended strongly on the contact resistance. Jeon et al. [15] proposed a detailed microstructural model and examined systematically the influence of the rib width, pitch width and area specific contact resistance ($ASR_{contact}$) on the stack-cell performance. The work by Jeon et al. provided very useful information in revealing the details of the complex interaction of competing factors in SOFC operations. Unfortunately, their optimization results appear to be dependent on a large number of design and operational parameters and are difficult to generalize and to provide easy-to-use design guidance to the broad fuel cell engineering society. Moreover, their treatment of the effective in-plane area specific resistance appears to be oversimplified and may affect the optimization result for the cathode current collect layer thickness.

In the present study, the cell performance of an SOFC stack is analyzed with a mathematical model capable of describing the details of gas transport in the electrodes, electronic and ionic conductions in the MEA, the electrochemical reactions at the three phase boundaries (TPBs) and the current distributions in the stack-cell. The optimal rib designs for different combinations of pitch widths and $ASR_{contact}$ are obtained and parameterized to provide an easy-to-use guidance for optimizing the rib–channel layout. The applicability of the results to the stack operations is validated by sensitivity analysis for a range of hydrogen concentrations. The generality of the results for different fuel cells is illustrated by testing on electrodes with different thickness, different porosity and different conductivities. The influence of the cathode thickness on the performance of a fuel cell stack is also examined.

2. Method

We limit ourselves to the discussion of anode-supported planar SOFC stacks with co-flow or counter flow designs to simplify the two-dimensional (2D) model setup. The modeling results for the rib size optimization might be similar for the cross-flow design as the obtained results to be discussed below are only sensitive to the rib-electrode contact resistance. A schematic cross-section of a repeating unit is sketched in Fig. 1. The fuel and oxidant gases are supplied to the cell through the channel/electrode boundary and the current is collected through the rib. As the TPBs are effective only at the region very close to the electrode/electrolyte interfaces, the TPBs are assumed to be located only at the electrode/electrolyte interfaces and there are no electrochemical reactions inside the electrodes in our numerical model. Though metallic interconnects with high conductivities are the desired and frequently used materials for the bipolar current collectors, the contact resistance at the rib and electrode boundary may be substantial due to the formation of oxide scales. Many efforts are devoted to the reduction of the area specific contact resistance of low cost alloy interconnects, such as Ni-, Fe-, and Co-based superalloys, Cr-based alloys, and stainless steel, to the desired level of 25–50 $m\Omega\,cm^2$ [16,20,21]. At the desired level of contact resistance, the fuel cell performance may still be significantly affected and the design optimization is important. The general approach in discussing the rib effects is to map out the transportation process in the case of rib presence, starting from the known parameters when ribs are absent. The gas transportation path determines the concentration polarization and electrochemical performance, and the electrical path determines the ohmic polarization. The overall cell performance as well as the optimal rib design can then be determined.

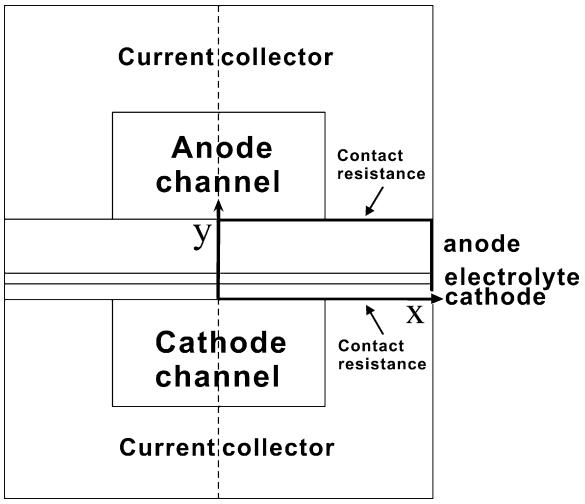

Fig. 1. Schematic cross-section of a repeating unit in a planar SOFC stack.

2.1. Physical model

Due to symmetry reason, only half of the repeating unit shown in Fig. 1 needs to be examined. Furthermore, the gas channels and the bipolar plate can be replaced with the proper boundary conditions for gas transport and electric potential. The contact resistance is set on the boundary of interconnect ribs and electrodes. With good connection between interconnect and electrode materials, the contact resistance is dominated by the oxide scale of the interconnect [16,20,21] and is assumed here to be uniform in the rib region. Moreover, the $ASR_{contact}$ on the anode side and on the cathode side are set to be the same in our model and is equivalent to the average $ASR_{contact}$ of the anode and cathode sides as the total currents for the anode and cathode ribs are identical. In our calculations for the thin cathode layer stacks, it is noticed that part of the cathode area underneath the interconnect rib may run out of gas at high current density. The gas depletion zone may cause numerical instability in simulating the gas transport process as the boundary condition derived from the electrochemical reaction may cause negative oxygen concentration there. Similar numerical instability has been encountered by other researchers [15]. To overcome the numerical difficulty, the gas depletion area may be identified with a cutoff gas pressure ($0.5\%\,p_{O_2}$) and treated as a pure electric conducting area. The cutoff pressure has been verified to cause negligible error in the result. For example, the average output current density for the baseline case with rib width of 0.8 mm to be described in Section 3.1 is 0.5143 and 0.5145 $A\,cm^{-2}$ for the cutoff gas pressure of 0.5% and 0.1%, respectively. Except the pure conducting area, the cathode is treated as the usual gas diffusion and electric conduction area. As a result, the overall physical model is reduced to that shown in Fig. 2. For easy description of boundary conditions in later part of the paper, each boundary line segment in our 2D model is assigned with an alphabetic name as indicated in Fig. 2.

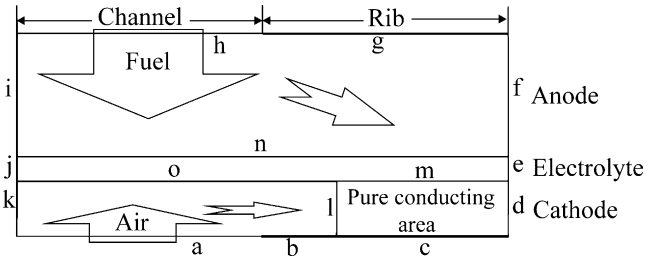

Fig. 2. Sketch of the physical model and subdomains and boundary designations.

The overall cell performance can be described by the operating cell potential and the output current. The operating cell potential (V_{cell}) can be formally expressed as:

$$V_{cell} = E_0 - \eta_{ASR;a} - \eta_{conc;a} - \eta_{act;a} - \eta_{ohm;a} - \eta_{ohm;el} - \eta_{ohm;c} - \eta_{act;c} - \eta_{conc;c} - \eta_{ASR;c} \quad (1)$$

where E_0 is the Nernst potential, $\eta_{conc;a}$ and $\eta_{conc;c}$ are respectively the concentration overpotentials at the anode and the cathode due to the gas species diffusion resistance, $\eta_{act;a}$ and $\eta_{act;c}$ the corresponding activation overpotentials, $\eta_{ohm;a}$, $\eta_{ohm;el}$ and $\eta_{ohm;c}$ the ohmic overpotentials in the anode, electrolyte and cathode, $\eta_{ASR;a}$ and $\eta_{ASR;c}$ the anode and cathode interface overpotentials due to the contact resistance at material boundaries. All these overpotentials are functions of the current density, j. Models for each of the overpotentials will be described in subsequent sections in the paper. As V_{cell} is an operating parameter, V_{cell} is used as an appropriate boundary condition for solving the current density distribution in the physical model.

The average output current density of the SOFC stack can be calculated by

$$\bar{j} = \frac{1}{d_{pitch}} \int_{x=0}^{d_{pitch}} j_y \, dx \quad (2)$$

where d_{pitch} is the pitch width (the sum of the rib width, d_{rib}, and the channel width, $d_{channel}$). The x- and y-axis are along the horizontal and vertical directions in the 2D model, respectively. j_y is the y component of the current density flux vector.

2.2. Gas transport modeling

The gas flow transports in the anode and cathode are governed by the momentum and mass balance equations.

2.2.1. Momentum balance equation

In the porous structure of electrodes, the gas flow is mainly driven by the pressure gradient. The Darcy's law and the continuity equation were used to simulate the flow in electrodes

$$u = -\frac{k}{\eta} \nabla p \quad (3a)$$

$$\nabla \cdot \rho u = 0 \quad (3b)$$

where k denotes the permeability of the porous media (m^2), η the fluid viscosity (Pa s), p the pressure (Pa), u the velocity vector ($m\,s^{-1}$) and ρ is the density of the fluid ($kg\,m^{-3}$). The density of fuel (ρ_f) and air (ρ_{air}) are calculated by the gases molar fractions

$$\rho_f = \frac{p(x_{H_2} M_{H_2} + x_{H_2O} M_{H_2O})}{RT} \quad (4a)$$

$$\rho_{air} = \frac{p(x_{O_2} M_{O_2} + x_{N_2} M_{N_2})}{RT} \quad (4b)$$

where M_i is the molar mass of species i, x_j the molar fraction of species j, R the universal gas constant and T is the temperature.

The anode concentration overpotential is related to the partial pressures of fuel species by $\eta_{conc;a} = (RT/2F)\ln((p_{H_2,f}/p_{H_2O,f})(p_{H_2O,TPB}/p_{H_2,TPB}))$, where F is the Faraday constant. The anode concentration overpotential depends on the x coordinate of the TPB in anode. Similarly, the cathode concentration overpotential is related to the oxygen partial pressures by $\eta_{conc;c} = (RT/4F)\ln(p_{O_2,air}/p_{O_2,TPB})$ and depends on the x coordinate of the TPB in cathode. In this article, subscript a, c, el, I, air, f and TPB refers to anode, cathode, electrolyte, interconnect, air, fuel and TPB, respectively. As the Nernst potential is given as

$$E_0 = E_0^0 + \frac{RT}{2F}\ln\left(\frac{p_{H_2,f}}{p_{H_2O,f}}\right) + \frac{RT}{4F}\ln\left(\frac{p_{O_2,air}}{1\,atm}\right) \quad (5)$$

where E_0^0 is the Nernst potential when the partial pressure of H_2, H_2O and O_2 are all at 1 atm (and $E_0^0 = 1.01$ V at $T = 973$ K or 700 °C), the last two terms of Eq. (5) can be combined with $\eta_{conc;a}$ and $\eta_{conc;c}$, respectively, to yield the anode and cathode balance potentials:

$$\eta_a^0 = -\frac{RT}{2F}\ln\left(\frac{p_{H_2,a}}{p_{H_2O,a}}\right)\Bigg|_{TPB} \quad (6a)$$

$$\eta_c^0 = -\frac{RT}{4F}\ln\left(\frac{P_{O_2,c|TPB}}{1\,atm}\right) \quad (6b)$$

Eq. (1) may then be rewritten as

$$V_{cell} = E_0^0 - \eta_{ASR;a} - \eta_a^0 - \eta_{act;a} - \eta_{ohm;a} - \eta_{ohm;el} - \eta_{ohm;c} - \eta_{act;c} - \eta_c^0 - \eta_{ASR;c} \quad (1')$$

2.2.2. Mass balance equation (Maxwell–Stefan equation)

In the SOFC porous electrodes, the relative concentrations of gas species are of the same order of magnitude. The Maxwell–Stefan equation is suitable for calculating the gas transport processes. The governing equation is

$$\nabla \cdot \left(\rho\omega_i u - \rho\omega_i \sum_{j=1}^{n} \tilde{D}_{ij}(\nabla x_j + (x_j - \omega_j)\frac{\nabla p}{p})\right) = 0 \quad (7a)$$

$$\sum_{i=1}^{n} \omega_i = 1 \quad (7b)$$

where ω_i is the mass fraction of species i.

$\tilde{D}$ is the multi-component Fick diffusivity. It is related to the multi-component Maxwell–Stefan diffusivity (D) by the expressions [22]

$$\tilde{D}_{11} = \frac{\omega_2^2}{x_1 x_2} D_{12} \quad (8a)$$

$$\tilde{D}_{12} = \tilde{D}_{21} = -\frac{\omega_1 \omega_2}{x_1 x_2} D_{12} \quad (8b)$$

$$\tilde{D}_{22} = \frac{\omega_1^2}{x_1 x_2} D_{12} \quad (8c)$$

The multi-component Maxwell–Stefan diffusivity can be calculated by the expression [23]

$$D_{ij} = 3.198 \times 10^{-8} \times \frac{T^{1.75}}{p(v_i^{1/3} + v_j^{1/3})^2}\left[\frac{1}{M_i} + \frac{1}{M_j}\right]^{1/2} \quad (9)$$

where v_i is the diffusion volume for species i. In porous media, the effective diffusivity is reduced to [24]

$$D_{ij}^{\text{eff}} = \varepsilon^{\tau} D_{ij} \tag{10}$$

where ε is the porosity and τ the tortuosity of the porous media.

2.3. Electric current transport

The electrical current is determined by the charge balance equation. Electronic charge transfer equation was used to obtain the current distribution in the anode and cathode area

$$-\nabla \cdot (\sigma_e \nabla V_e) = 0 \tag{11a}$$

where σ_e is the electronic conductivity of the electrode material and V_e the electric potential in the electrode and $-\sigma_e \nabla V_e$ the flux vector of the electronic current density. The difference between the electric potentials along the electronic current flux path at the electrode-rib boundary and the TPB-electrode boundary is the electrode ohmic polarization ($\eta_{\text{ohm;a}}$ or $\eta_{\text{ohm;c}}$) and is generally current path dependent.

Ionic charge transfer equation was used in the electrolyte

$$-\nabla \cdot (\sigma_i \nabla V_i) = 0 \tag{11b}$$

where σ_i is the ionic conductivity of the electrolyte, V_i the electric potential in the electrolyte and $-\sigma_i \nabla V_i$ is the flux vector of the ionic current density. The difference between the electric potentials along the ionic current flux path at the electrolyte-anode boundary and the electrolyte-cathode boundary is the electrolyte ohmic polarization ($\eta_{\text{ohm;el}}$) and is also current path dependent.

The electric potential loss inside interconnect plate is assumed to be negligible due to high conductivity of the metallic material. The local current densities cross the interconnect/anode ($j_{\text{I}\to\text{a}}$) and the cathode/interconnect ($j_{\text{c}\to\text{I}}$) interfaces are determined by the associated electric potential changes, or the interface overpotentials:

$$j_{\text{I}\to\text{a}} = \frac{V_{\text{e,I/a}} - V_{\text{e,a/I}}}{\text{ASR}_{\text{contact}}} = \frac{\eta_{\text{ASR;a}}}{\text{ASR}_{\text{contact}}} \tag{11c}$$

$$j_{\text{c}\to\text{I}} = \frac{V_{\text{e,c/I}} - V_{\text{e,I/c}}}{\text{ASR}_{\text{contact}}} = \frac{\eta_{\text{ASR;c}}}{\text{ASR}_{\text{contact}}} \tag{11d}$$

where $V_{\text{e,I/a}}$ and $V_{\text{e,a/I}}$ are respectively the interconnect and anode electric potentials at the anode-interconnect boundary, $V_{\text{e,c/I}}$ and $V_{\text{e,I/c}}$ the cathode and interconnect electric potentials at the cathode-interconnect boundary.

2.4. The current density at the TPB

The current density at the TPB is proportional to the electrochemical reaction rates. It is related to the exchange current density, the partial pressure and the activation polarization (overpotential) by the Butler–Volmer equation. However, different parameterization forms have been proposed based on different experimental measurements. As long as an expression is able to represent the experimental data reasonably well, the specific form is not critical due to the use of fitting parameters.

According to the empirical forms suggested before [15,25–27], the Butler–Volmer equation used here for the anode side TPB is expressed as

$$j_a = \begin{cases} j_{0,a}\left(\dfrac{p_{H_2,TPB}}{p_{H_2,f}}\right)^{0.11}\left(\dfrac{p_{H_2O,TPB}}{p_{H_2O,f}}\right)^{0.67}\left[\exp\left(\dfrac{2F\eta_{act,a}}{RT}\right) - \exp\left(\dfrac{-F\eta_{act,a}}{RT}\right)\right] & \text{for } p_{H_2O,TPB} < 14,000\,\text{Pa} \\ j_{0,a}\left(\dfrac{p_{H_2,TPB}}{p_{H_2,f}}\right)^{0.11}\left(\dfrac{14,000}{p_{H_2O,f}}\right)^{0.67}\left[\exp\left(\dfrac{2F\eta_{act,a}}{RT}\right) - \exp\left(\dfrac{-F\eta_{act,a}}{RT}\right)\right] & \text{for } p_{H_2O,TPB} \geq 14,000\,\text{Pa} \end{cases} \tag{12a}$$

where j_a is the current density and $j_{0,a}$ the exchange current density for the anode TPB. The cutoff pressure of 14,000 Pa for $p_{H_2O,TPB}$ is used to account for the catalytic effect of water vapor [28].

The Butler–Volmer equation used for the cathode side TPB is [26,29,30]

$$j_c = j_{0,c}\left(\frac{p_{O_2,TPB}}{p_{O_2,air}}\right)^{1/2}\left[\exp\left(\frac{2F\eta_{act,c}}{RT}\right) - \exp\left(\frac{-2F\eta_{act,c}}{RT}\right)\right] \tag{12b}$$

where $j_{0,c}$ is the exchange current density for the cathode TPB.

The activation polarizations, $\eta_{act,a}$ and $\eta_{act,c}$, are related to the electric and balance potentials by

$$\eta_{act,a} = V_{e,a/el} - V_{i,el/a} - \eta_a^0 \tag{13a}$$

$$\eta_{act,c} = V_{i,el/c} - V_{e,c/el} - \eta_c^0 \tag{13b}$$

where $V_{e,a/el}$ and $V_{i,el/a}$ are respectively the anode and electrolyte electric potentials at the anode-electrolyte boundary, $V_{i,el/c}$ and $V_{e,c/el}$ the electrolyte and cathode electric potentials at the cathode-electrolyte boundary.

2.5. Boundary conditions (BCs)

As described above, the governing partial differential equations (PDEs) are Darcy's law and Maxwell–Stefan equation for the gas diffusions in the anode and cathode, Ohm's law for electrical current conduction in the anode, cathode and electrolyte. The settings for the boundary conditions required for solving these PDEs are summarized in Tables 1 and 2.

The Butler–Volmer equations are coupled with the governing equations and provide the current densities at the TPB boundaries for given gas concentrations and activation overpotentials. The current densities then serve as the boundary conditions to solve the governing equations, resulting in new TPB gas concentrations and activation overpotentials. The iterative process continues until a convergent solution is found.

2.6. Basic model parameters

Unless stated otherwise, the following model parameters are used. Cell operates at $T = 973$ K (700 °C) with both fuel and air at

Table 1
Boundary settings for Darcy's law and the Maxwell–Stefan equation

	Boundary	a	h	o	n	All others
Darcy's law	BC type	Pressure condition		Velocity inflow/outflow	Velocity inflow/outflow	Insulation/symmetry
	BC	1 atm		$\frac{j_a}{2F\rho_f}(M_{H_2O} - M_{H_2})$	$\frac{-j_c}{4F\rho_{air}}M_{O_2}$	
Maxwell–Stefan equation	BC type	(O_2) mass fraction	(H_2) mass fraction	(O_2) flux	(H_2) flux	Insulation/symmetry
	BC	0.23 (air)	$\omega_{H_2}^0$	$\frac{-j_c M_{O_2}}{4F}$	$\frac{-j_a M_{H_2}}{2F}$	

Table 2
Boundary settings for the electronic and ionic charge transfer equations

	Boundary	b, c	g	o	n	m	All others
	BC type	Reference potential	Reference potential	Inward current flow	Inward current flow	Inward current flow	Electric insulation
Electronic	BC	$V_{cell} - E_0^0$	0	j_c	$-j_a$	0	
Ionic	BC			$-j_c$	j_a	0	

pressure of 1 atm. The molar fraction of hydrogen in the fuel is 0.90. The output cell voltage is fixed at 0.7 V, a balanced choice for cell efficiency and power density [24]. The viscosities for fuel and air are respectively 2.8×10^{-5} and 4×10^{-5} Pa s [24,31]. The diffusion volumes for H_2, H_2O, O_2 and N_2 are 7.07×10^{-6}, 12.7×10^{-6}, 16.6×10^{-6} and 17.9×10^{-6} m^3 mol^{-1}, respectively [32]. Anode permeability and cathode permeability are respectively 1.7×10^{-10} and 1×10^{-13} m^2 [31,33]. The thicknesses for anode, cathode and electrolyte layers are 750, 50 and 10 μm, respectively. Anode porosity is 0.38 and cathode porosity is 0.3. Both anode and cathode tortuosities are 3. The anode and cathode exchange current densities are 4280 and 1070 A m^{-2}, respectively. The expressions for anode, cathode and electrolyte conductivities (s m^{-1}) are $\sigma_a = 3.356 \times 10^4 \exp(1392/T)$, $\sigma_c = 1.223 \times 10^4 \exp(-600/T)$ and $\sigma_{el} = 3.34 \times 10^4 \exp(-10{,}300/T)$, respectively [17,34]. The fuel cell described with these parameters is sometime referred as the reference cell for convenience.

2.7. Numerical solutions

The finite element commercial software COMSOL MULTIPHYSICS® Version 3.4 [35] was used in the present study to solve the PDEs with the appropriate boundary settings. The COMSOL stationary nonlinear solver uses an affine invariant form of the damped Newton method [36] to solve the discretized PDEs with a relative tolerance of 1×10^{-6}. Fine triangle meshes were used and verified to provide accurate results in comparison with the very fine mesh of a maximum element size of 1×10^{-5} m for boundaries a, b and c and 0.5×10^{-6} m for region around the a and b contact area. The output current densities for various combinations of cell designs and operating parameters were calculated. As many calculations were involved, the COMSOL Script 1.2 [35] was employed to carry out the algorithm more efficiently. The examined hydrogen molar concentrations in the fuel were 0.97, 0.9, 0.6 and 0.29. These values may be used to represent hydrogen depletion as hydrogen flow down the channel. The rib effects on the stack operations were evaluated with the specific area contact resistances of 1×10^{-5}, 0.01, 0.025, 0.05, 0.075, and 0.1 Ω cm^2 for the interconnect-electrode contacts. Unless stated otherwise, the specific area contact resistance of 0.05 Ω cm^2 is used for the interconnect-electrode contacts. The pitch width was varied from 0.5 to 5 mm in step of 0.5 mm. For a given pitch width, the optimized rib width was found by varying the channel width to produce the maximum output power. The sensitivity of the optimization results on various factors such as the cathode thickness, porosity and conductivity were also tested. The effects of cathode thickness on the cell performance were examined by varying the cathode thickness from 50 to 400 μm. Single cell performance used below are calculated using the model without pure conducting area and no contact resistance, and all the pitch

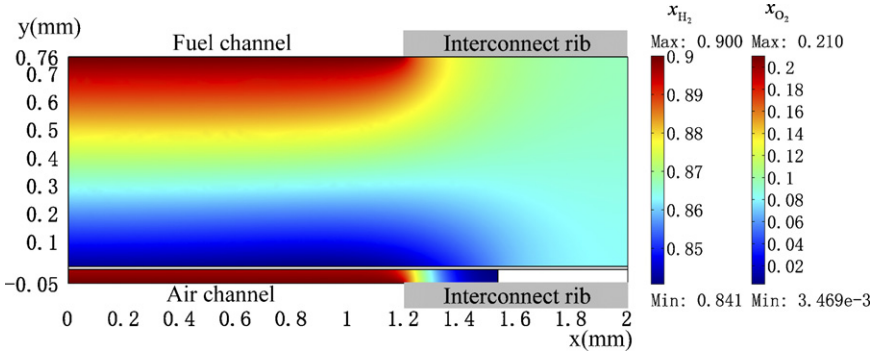

Fig. 3. Distributions of hydrogen and oxygen molar fractions (x_{H_2}, x_{O_2}).

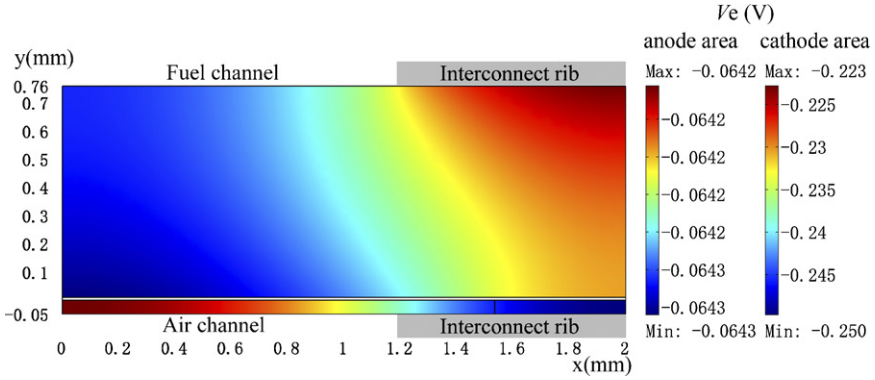

Fig. 4. The distributions of the anode and cathode electric potentials.

(channel and rib) boundaries were set as gas inlet/outlet and electric conductive boundaries.

3. Results and discussion

3.1. Performances of cells with ribs

We begin by showing specific examples of the effects of rib designs on the fuel cell performances. The pitch and rib widths for the stack cell are 2 and 0.8 mm, respectively. With these settings, the mean output current density for the reference cell was calculated to be 0.51 A cm^{-2}, a significant reduction from the result of 1.4 A cm^{-2} for the single cell without the ribs.

Fig. 3 shows the hydrogen and oxygen molar fraction distributions over the anode and cathode, respectively. The H_2 molar fraction varies over the range of 0.84–0.90. The maximum H_2 molar fraction is naturally at the channel-anode boundary, and the minimum is at the TPB underneath the channel. The rib effect on the anode gas transport is quite limited. While for cathode, an oxygen depletion zone with a width of 0.46 mm (23% of the pitch width) was identified. This oxygen depletion zone alone would contribute to 23% reduction of the cell output. As shown in Fig. 3, the oxygen concentration is very low in the diffusion region neighboring the depletion zone, further contributing to the reduction of the stack cell performance. The diffusion of oxygen is much easier than hydrogen in the vertical direction due to the relative short diffusion path. In the horizontal direction, however, the oxygen diffusion is limited by the relative narrower alleyway which is direct proportion to the cathode thickness, and may be depleted easily when the output current is not small.

Fig. 4 shows the electric potential distribution in the anode and cathode. As stated above (see Table 3), the reference potential at the rib-anode boundary was 0 V and at the rib-cathode boundary $V_{cell} - E_0^0 = -0.31$ V. As can be seen, the potential loss due to the anode-rib contact resistance was about 64 mV and the anode side potential variation is very small. Notable potential variation is observed in the cathode. The potential loss due to the cathode-rib contact resistance varied from 60 to 72 mV. The cathode potential varied from −0.250 to −0.223 V and the maximum potential change inside cathode was 27 mV. The ohmic overpotentials due to the rib-electrode contacts are significant contributors to the reduction of the stack cell performance. The cathode ohmic overpotential is also big enough to influence the cell output.

Table 3
Parameters for the optimal rib width, Eq. (14), for various $ASR_{contact}$ (Ω cm^2)

$ASR_{contact}$	10^{-5}	0.005	0.01	0.025	0.05	0.075	0.1
A (mm)	0.067	0.077	0.078	0.083	0.092	0.101	0.107
B	0.043	0.158	0.211	0.296	0.370	0.415	0.448

As the cathode conductivity is relatively high, large cathode ohmic overpotential is somewhat unexpected. It becomes clear when the distribution of the current flux is displayed. Fig. 5 shows the distributions of the current densities and flux vectors in the anode and cathode areas. The total current densities in the cathode are much larger than the stack cell output current density. For the current generated in the TPB zone to reach the cathode interconnect, most of the current has to flow along the horizontal direction with a narrow cross-section defined by the cathode thickness and a long path length determined by the channel width. Consequently, the cathode ohmic overpotential for the stack cell (~10 mV) is several orders of magnitude higher than that for a single cell with Pt or Ag mesh as current collector (~0.04 mV). As noted by passing, the current density around the cathode, channel and rib boundary zone is particularly high and may be a significant heat source and cause mechanical failures. More attentions should be paid to the area in the process of evaluating the mechanical performance of the fuel cell stack.

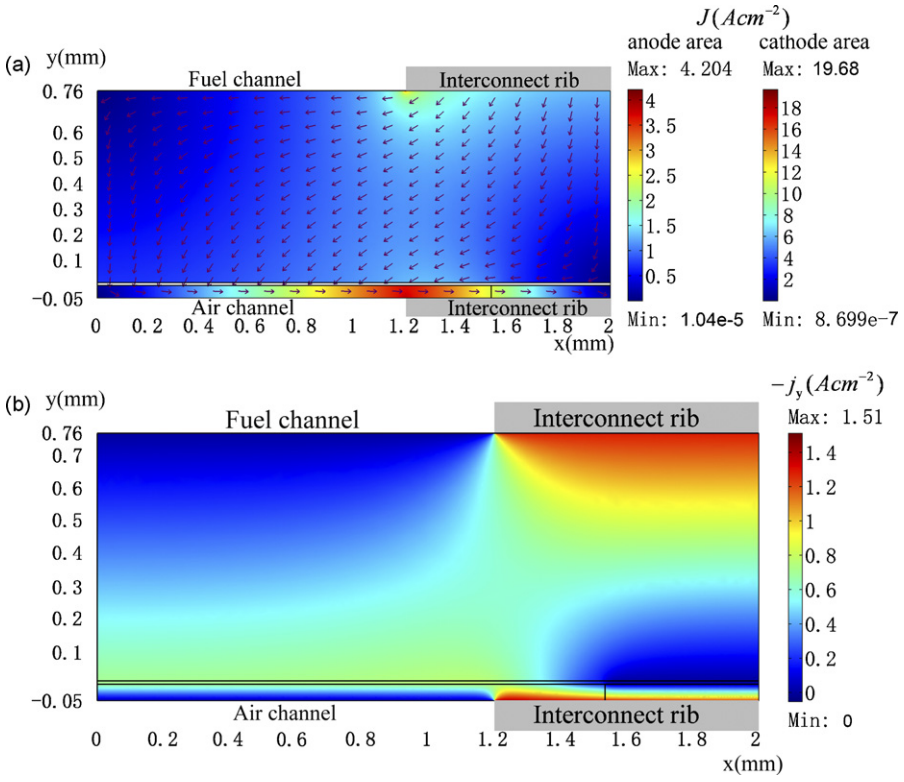

Fig. 5. The current density distributions: (a) the current density and current flux vector in the electrodes; (b) the y-component of the current flux vector in the fuel cell.

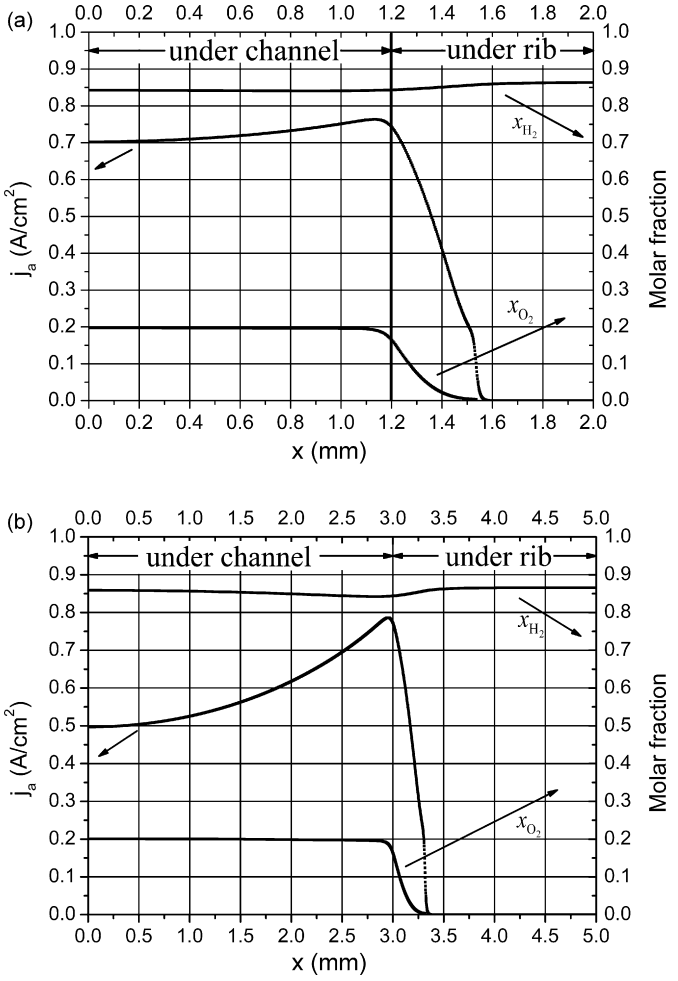

Fig. 6. Distributions of the TPB current density, H_2 and O_2 molar fractions: (a) d_{pitch} = 2 mm and d_{rib} = 0.8 mm; (b) d_{pitch} = 5 mm and d_{rib} = 2 mm.

Fig. 6 shows the hydrogen molar fraction and current density distributions at the anode TPB and the oxygen molar fraction distribution at the cathode TPB for two stack cell designs of: (a) d_{pitch} = 2 mm, d_{rib} = 0.8 mm and (b) d_{pitch} = 5 mm, d_{rib} = 2 mm. For the stack cell with d_{pitch} = 2 mm and d_{rib} = 0.8 mm, the current density in region underneath the channel (x < 1.2 mm) is quite uniform and varies between 0.70 and 0.76 A cm^{-2} with a maximum at x = 1.13 mm. The current density for the TPB underneath the rib (x > 1.2 mm) decreases rapidly with increasing x and is negligible for x > 1.6 mm. With increasing x for the TPB underneath the rib, the H_2 molar fraction increases slightly, while the O_2 molar fraction of oxygen decreases rapidly. Clearly, the TPB current density distribution is mainly determined by the oxygen concentration. For the stack cell design of d_{pitch} = 5 mm and d_{rib} = 2 mm that has the same rib to pitch width ratio as the former design of d_{pitch} = 2 mm and d_{rib} = 0.8 mm, the cell output current is reduced to 0.39 A cm^{-2}, a deduction of 24% from the cell output current density of 0.51 A cm^{-2} for the former design. The performance reduction is mainly due to the increased cathode current path length and the increased cathode ohmic overpotential for the increased channel width, as discussed above. With the wider pitch design, the TPB current density underneath the channel is less uniform and varies between 0.50 and 0.79 A cm^{-2}. The current density for the TPB underneath the rib (x > 3 mm) also decreases rapidly with increasing x and is determined by the corresponding TPB oxygen concentration.

It is worthy noting that the hydrogen concentrations at the anode TPB are quite similar in both designs. The effect of the rib presence in the anode side on the TPB current generation is completely dominated by the effect of the rib in the cathode side. As far as the hydrogen transport and the TPB current generation are concerned, the presence or absence of the anode rib is inconsequential. As the average electrical path for the cross-flow design is the same as the co- or counter-flow design, the numerical results in the present work may be also applicable to the cross-flow design.

3.2. Optimizations of the rib widths

Fig. 7a shows a contour map of the average cell current density as a function of the rib width and channel width for the reference cell. Generally, the smaller the pitch width ($d_{pitch} = d_{channel} + d_{rib}$, Fig. 7a is only for d_{pitch} < 4 mm), the higher is the output current density. For a given pitch width, there is an optimal rib width for producing the maximum cell current density, as can be seen in Fig. 7a. The maxima of current densities increase with the decrease of the pitch width. However, the pitch size may be limited by the manufacturing and engineering considerations. For a given pitch width as indicated by the dashed line in Fig. 7a ($d_{pitch} = d_{channel} + d_{rib}$ = constant), the output current density also depends strongly on the rib width and a suitable choice of the rib width is very important for the high

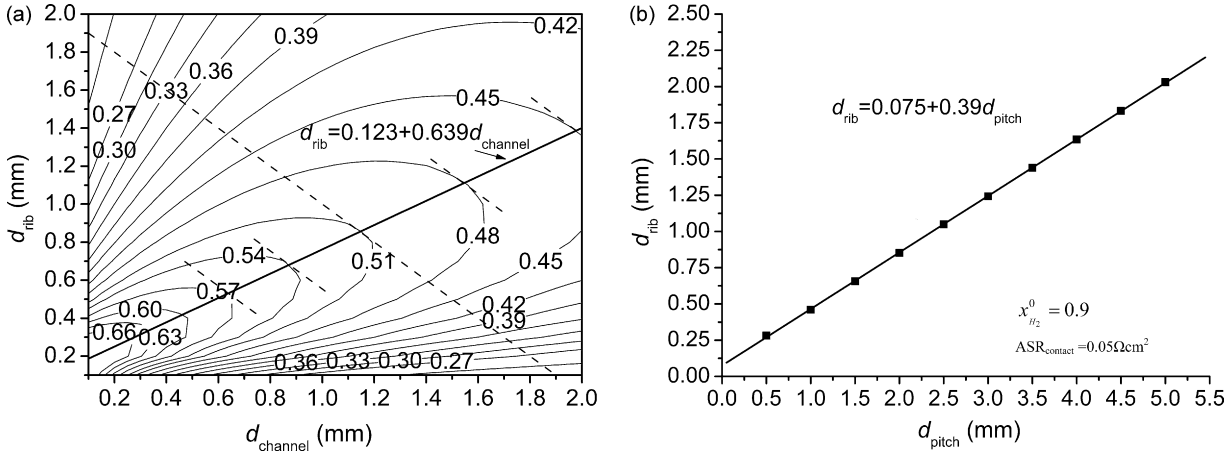

Fig. 7. The relationship between the cell output current density and the channel and rib widths: (a) the output current density vs. the channel width ($d_{channel}$) and the rib width (d_{rib}); (b) the channel widths for the maximum cell outputs vs. the pitch widths.

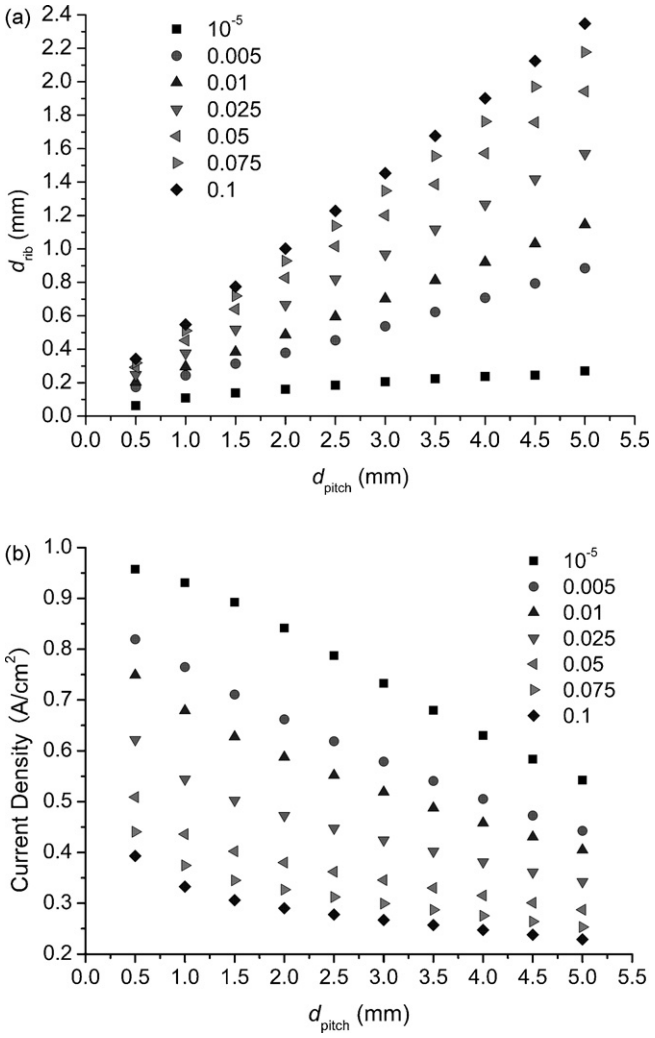

Fig. 8. The dependence of the optimal rib width and stack cell output on the pitch width for $ASR_{contact}$ varying from 10^{-5} to 0.1 Ω cm^2: (a) the optimized rib width vs. the pitch width and (b) the maximum output current density vs. the pitch width.

performance of a SOFC stack. The optimal rib width was found by varying the rib width for a given pitch width to produce the maximum output current density, which is the maximum on the corresponding dashed line. Fig. 7b shows the relationship between the given pitch width and the optimal rib width that produces the maximum cell output. It is interesting to note that the optimal rib width is linear to the pitch width and can be expressed as $d_{rib} = 0.075\,mm + 0.39 d_{pitch}$ ($0.5\,mm \le d_{pitch} \le 5\,mm$) for the reference cell with a contact resistance of 0.05 Ω cm^2.

3.2.1. The effect of $ASR_{contact}$ on the rib optimization

The optimal rib width is determined by the interplay between the gas transport and the current conduction. The higher the rib-electrode contact resistance, the higher the rib width is expected. Fig. 8a shows the relationship between the optimal rib width and the designated pitch width for a range of $ASR_{contact}$ varying from 10^{-5} to 0.1 Ω cm^2. To be more representative, the fuel with a medium hydrogen molar fraction of 0.6 is used here. As can be seen in Fig. 8a, the optimal rib width shows a high degree of linearity with the pitch width for any of the given $ASR_{contact}$, with the slope for the linearity decreases with the increase of $ASR_{contact}$. The corresponding current densities are also shown in Fig. 8b. For the small $ASR_{contact}$ of 10^{-5} Ω cm^2 and the small pitch width of 0.5 mm, the output current density is essentially the same as that for a single cell (0.97 A cm^{-2}) due to the fact that the optimal rib width is very small and the rib effects on ohmic overpotential and concentration overpotential are negligible. However, the rib effect cannot be ignored even for such small $ASR_{contact}$ when the pitch width is large. The output current density is reduced by over 40% for the pitch width of 5.0 mm. The performance degeneration is mainly due to the ohm loss of the cathode current conduction as shown in Fig. 5 and discussed above.

As shown in Fig. 8b, the output current density of the stack cell is severely influenced by the $ASR_{contact}$. Even for small pitch width of 1 mm and moderate $ASR_{contact}$ of 0.025 and 0.05 Ω cm^2, the optimal current densities are only 56% and 45% of that for the single cell, respectively. It is no surprise that the best reported stack cell output is less than half of that for the best single cell result.

3.2.2. The effect of hydrogen molar fraction on the rib optimization

As the cell may be fed with fuels with different hydrogen concentrations and the hydrogen concentration for a given fuel varies for different channel locations due to fuel consumption, the sensitivity test of the optimized rib width on the fuel composition is important for the rib design. The effects of inlet hydrogen molar fractions on the optimized rib widths and the output current densities vs. the pitch widths are shown in Figs. 9 and 10 for $ASR_{contact}$ of 0.05 Ω cm^2. Even though the stack cell output depends on the inlet hydrogen molar fraction, the influence of the inlet hydrogen molar fraction on the optimal rib width is quite limited. The results for $ASR_{contact}$ of 0.025 and 0.1 Ω cm^2 (not shown) provide the same conclusion. The optimal rib width is linear to the pitch width for any hydrogen molar fraction. For a given $ASR_{contact}$, the optimized rib widths are essentially the same for any hydrogen concentration when the pitch width is small. Even though the output current may vary substantially, the ratio of the optimal rib width to the pitch width changes by no more than 7% for any hydrogen concentration when taking the hydrogen molar fraction of 0.6 as the reference. The "insensitivity" of the optimal rib width to the H_2 concentration in fuel is in fact due to the "sensitivity" of the contact ohmic resistance overpotential to the rib width. The optimal rib size is due to the balance between the current collection and the gas transport. Smaller current output in general results in smaller optimal rib width, as can be seen in Figs. 9 and 10. In one hand, the contact ohmic overpotential is naturally sensitive to the rib width for high contact resistance

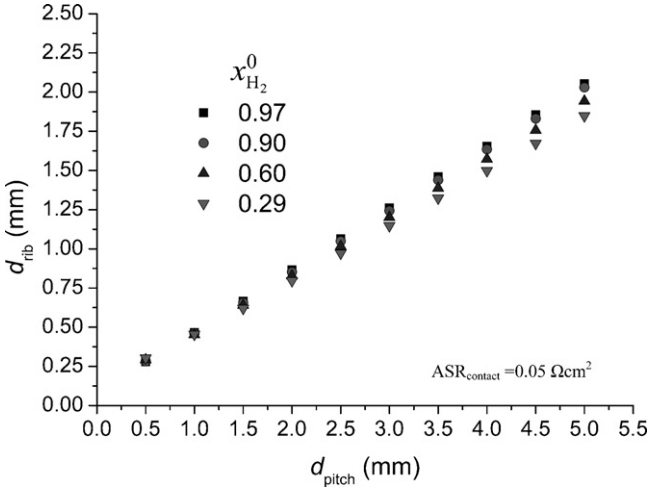

Fig. 9. Optimized rib width vs. the pitch width for different hydrogen concentrations in fuel and $ASR_{contact}$ = 0.05 Ω cm^2.

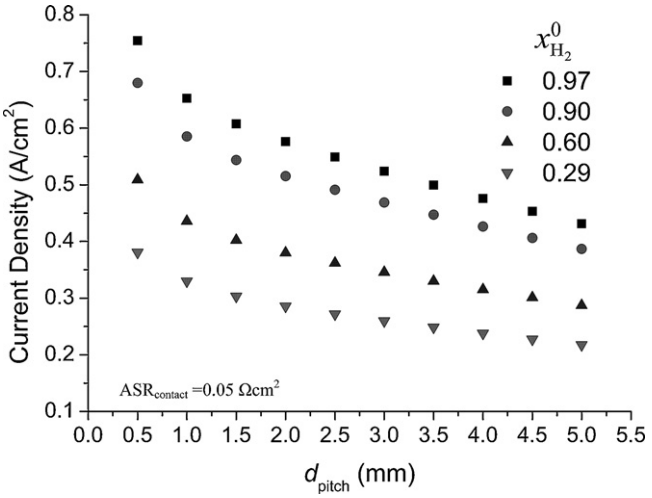

Fig. 10. The maximal output current density vs. the pitch width for different hydrogen concentrations in fuel and $ASR_{contact} = 0.05\ \Omega\ cm^2$.

rib. In the other hand, the optimal rib widths are relatively small for low contact resistance ribs. A small reduction of the rib width results in a relatively large increase of the ohmic overpotential with a small reduction of the transport overpotential. Consequently, the optimal rib widths for high and low hydrogen concentration fuels are not very different. This is fortunate as the optimized rib design is of general applicability for different fuel operations. As the H_2 molar fraction of 0.6 is roughly the average H_2 concentration in the cell channel for SOFC stacks operating with fuel of high H_2 molar fraction (say, 0.97) and desirable fuel utilization (say, 75%), the H_2 molar fraction of 0.6 is used in the following discussions in order to be more representative.

3.2.3. The effect of cathode porosity on the rib optimization

Fig. 11 compares the optimized rib widths and output current densities for cathodes with two different porosities, keeping all other material property parameters to be the same as the reference cell. Higher porosity is beneficial for the gas transport, resulting in larger output current and allowing for the use of wider ribs. Except for the rib with unrealistically low contact resistance, however, the optimal rib widths are essentially the same for the two porosities, as can be seen in Fig. 11a. The insensitivity of the optimal rib width is due to the dominant sensitivity of the ohmic overpotential to the rib width.

3.2.4. The effect of cathode layer thickness on the rib optimization

The rib width are also optimized for different cathode layer thickness varying from 50 to 400 μm. Except for cases with very small pitch widths, the optimal rib width is essentially independent of the cathode layer thickness. As shown in Fig. 12a, however, there may are appreciable variations in the output current densities in cases of large pitch widths. Reasonably thick cathode layer is beneficial for the oxygen transport to the TPB region underneath the rib area and helps to reduce the overall cell concentration overpotential, as can be seen by comparing Figs. 6a and 12b. Moreover, reasonably thick cathode layer is also beneficial for the reduction of the cathode ohmic overpotential by increasing the cross-section area for the current to pass through to reach the interconnect rib, as seen by comparing Figs. 5a and 12c. The nearly constant rib width is a result of the balance among the improved gas transport for wider rib, the increased current density for wider rib and the reduced cathode ohmic overpotential for narrower rib.

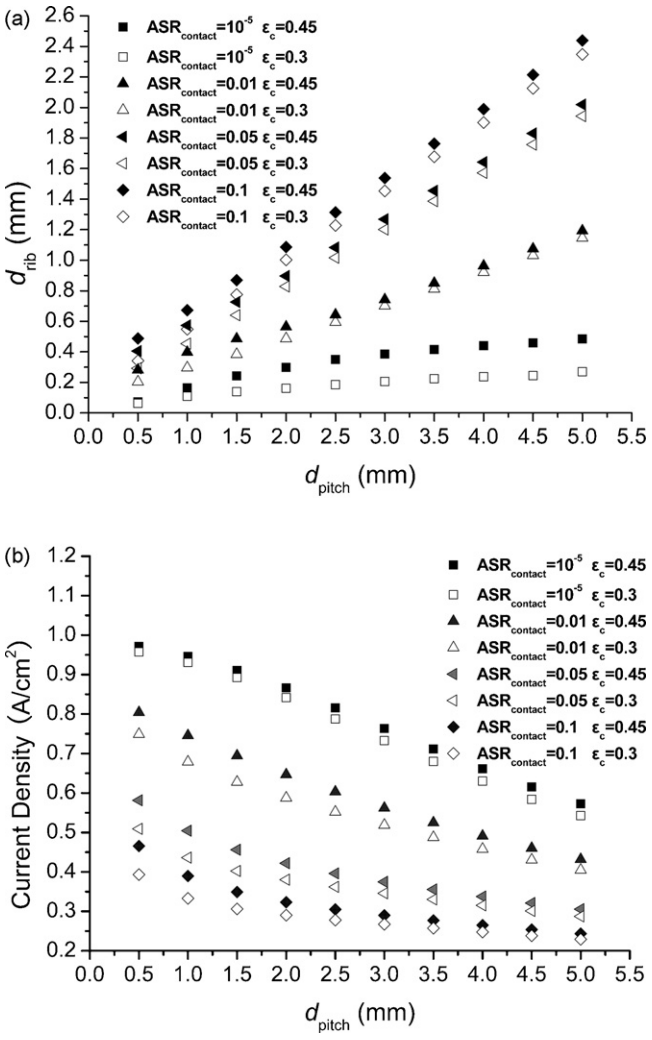

Fig. 11. Effects of cathode porosity on the optimal rib width and the cell output: (a) the optimal rib width vs. the pitch width; (b) the maximum current density vs. the pitch width.

3.2.5. The effect of cathode conductivity on the rib optimization

Due to the influence of various factors, e.g., porosity, conducting particle size and volume fraction, different layer structures, the effective cathode conductivity may vary for different designs. The effective cathode conductivities for practical cells [9,15] are similar to our reference value, differing by less than a factor of two. To examine the effects of the cathode conductivity on the rib design, four more conductivities corresponding to 1/5, 1/2, 2 and 5 times of our reference value are used in our simulations, while all other parameters are set at the reference values. Fig. 13 shows the results of the optimal rib widths and output current densities for these cathode conductivities. Except the case for the lowest conductivity and large pitch width, the effect of the cathode conductivity on the optimal rib width is small. The results may be attributed to the dominance of the rib contact ohmic overpotential over the cathode ohmic overpotential in typical cells. For the cathode with very low conductivity, lowering the cathode ohmic overpotential by shortening the current path is desired. Consequently, the optimal rib width for the wide pitch design is relatively large for the cathode with very low conductivity in comparison with the high conductivity cathode. Nevertheless, such low conductivity is not typical for practical cells. That is, the optimal rib width is practically independent of the cathode conductivity.

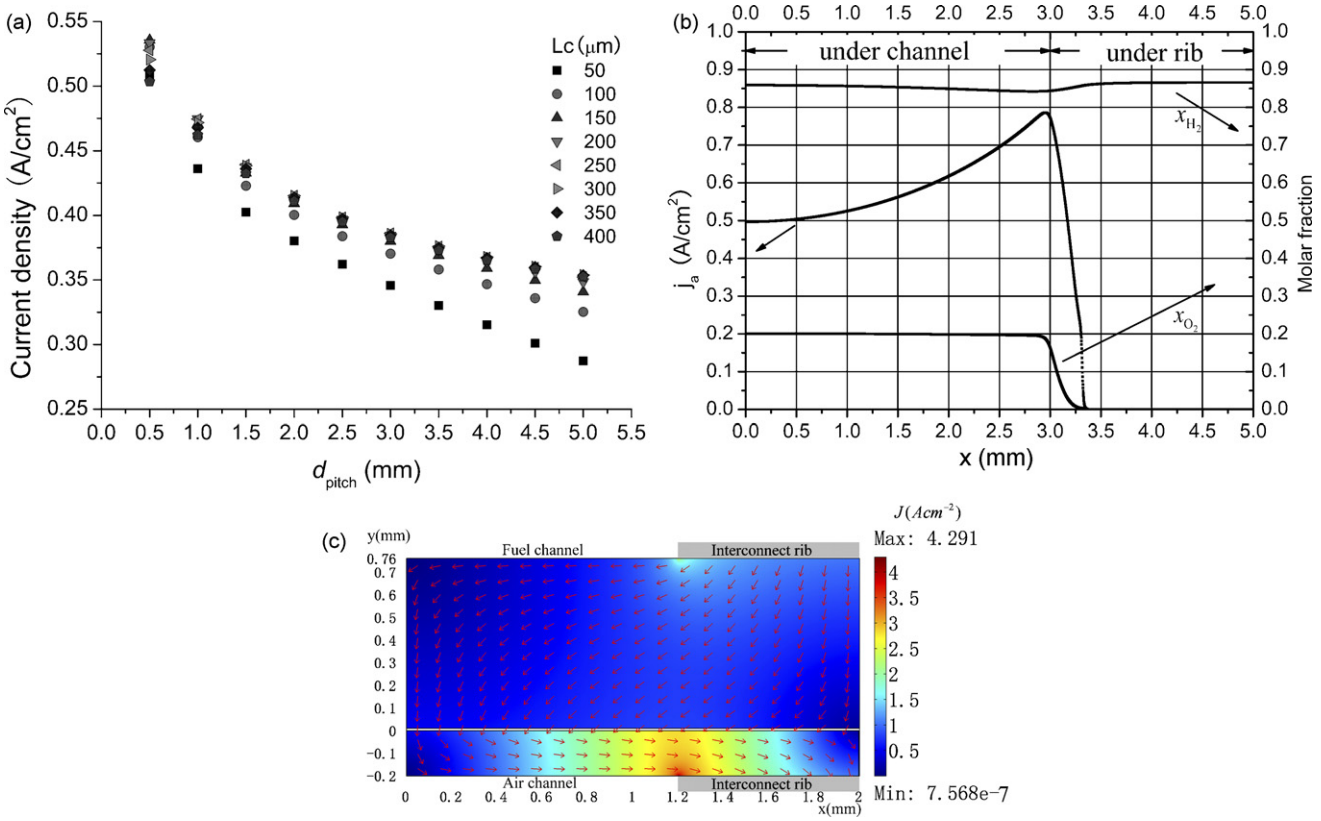

Fig. 12. The output current density for different cathode layer thicknesses (L_c) with the optimal rib width: (a) the maximum output current density vs. the pitch width; (b) distributions of the TPB current density and O_2 molar fraction for L_c = 200 μm and d_{pitch} = 2 mm; (c) the current density (A cm^{-2}) and current flux vector in the electrodes for L_c = 200 μm and d_{pitch} = 2 mm.

3.2.6. Parameters for the optimal rib designs

As discussed above, the optimal rib width for maximum cell output depends linearly on the pitch width, i.e.

$$d_{rib} = A + B \times d_{pitch} \quad (14)$$

The intercept, *A*, and the slope, *B*, are weakly dependent on the hydrogen molar fraction in the fuel and are essentially independent on the cathode porosity, the cathode layer thickness and the cathode conductivity. *A* and *B*, however, are dependent on the rib-electrode contact resistance that varies with materials as well as processing processes. As an easy to use engineering design guidance, Table 3 lists the parameters *A* and *B* based on the hydrogen molar fraction of 0.6 in the fuel for a range of $ASR_{contact}$ covering the cases for basically no contact resistance to fairly high contact resistance. For practical SOFC stacks, $ASR_{contact}$ is expected to be between 0.025 and 0.075 Ω cm^2 and the parameters for $ASR_{contact}$ of 0.05 Ω cm^2 may be viewed as generally representative for optimal designs. The parameters for $ASR_{contact}$ larger than 0.1 Ω cm^2 can in principle be obtained by extrapolation, but stacks with such $ASR_{contact}$ may be of limited practical use.

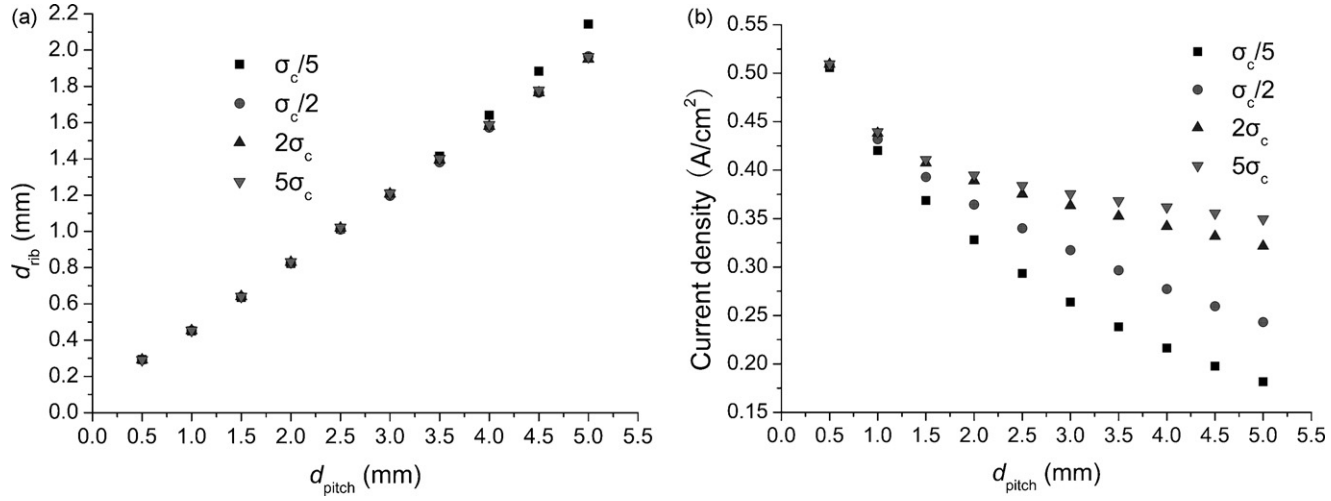

Fig. 13. The optimal rib width and output current density for four cathode conductivities varying from 1/5 to 5 times of the reference conductivity (σ_c): (a) the optimized rib width vs. the pitch width; (b) the maximum output current density vs. the pitch width.

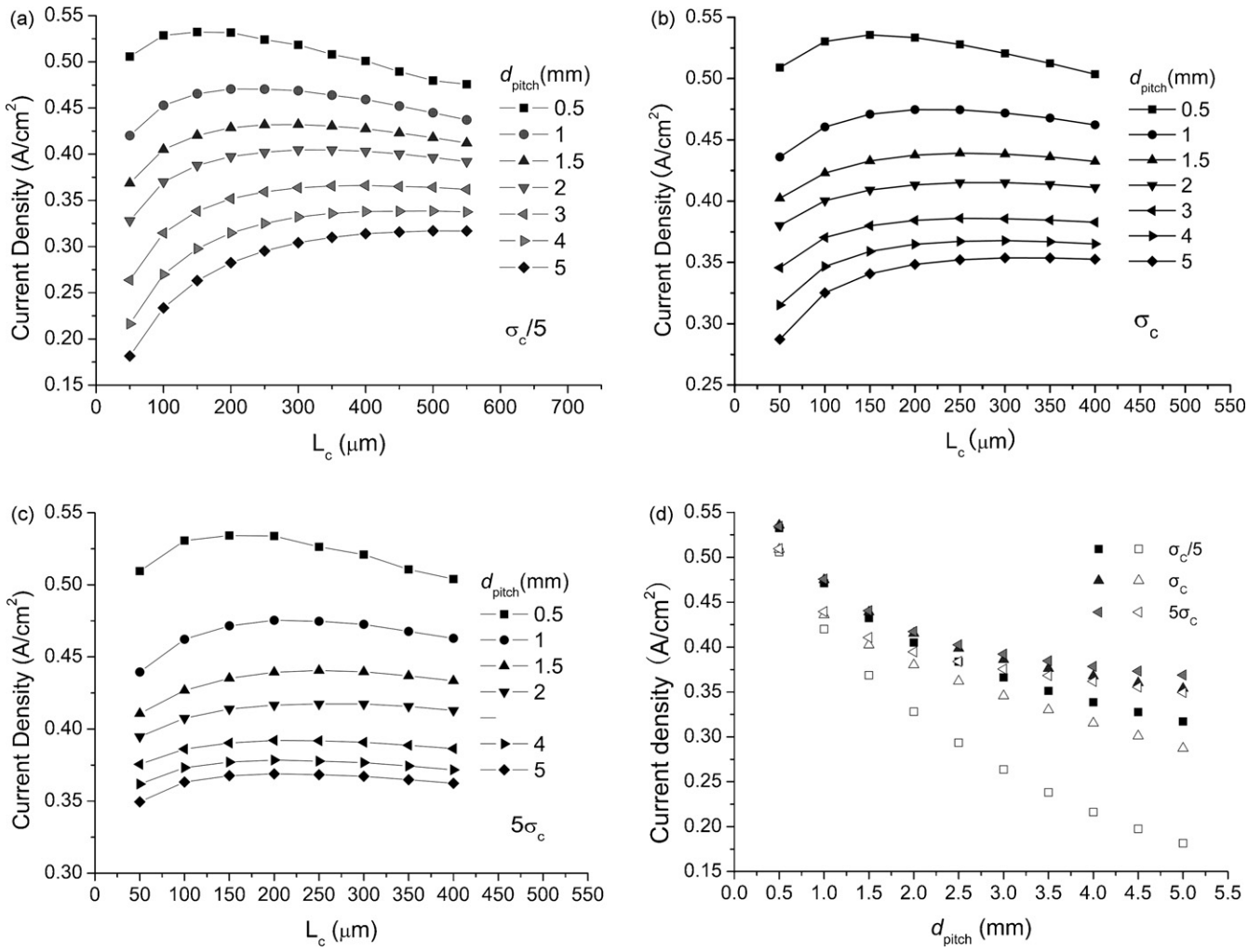

Fig. 14. The output current density as functions of the pitch width and cathode thickness for difference cathode conductivities: (a) $\sigma_c/5$; (b) σ_c; (c) $5\sigma_c$; (d) the maximum output current density vs. the pitch width, where the solid and open symbols are for the optimized cells and the cells with the cathode layer thickness of 50 μm, respectively.

3.3. Effect of the cathode layer thickness on the fuel cell performance

For anode supported SOFCs, thin cathode layer with thickness of about 50 μm is typical for sake of easy oxygen transport [2]. The concept is valid only when metallic mesh with good contact is used as the current collector that corresponds to negligible contact resistance and very small pitch width. For practical interconnect material in SOFC stack, the contact resistance is substantial and the rib width cannot be made too small. As discussed above, reasonably thick cathode layer is beneficial for oxygen transport to the TPB underneath the rib as well as for broadening the cross-section for current passage. As shown in Fig. 12a, the benefits may result in substantially higher current output for practical pitch width. Naturally, the two benefits should be balanced with the oxygen transport to the TPB region underneath the channel that prefers thinner cathode layers. Therefore, the optimization of the cathode layer thickness is of importance for the SOFC stack design.

Fig. 14 shows the output current density as functions of the pitch width and cathode thickness for three cathode conductivities corresponding to 1/5, 1 and 5 times of the reference value, while other parameters were the same as the reference cell and the rib width optimized. The results corresponding to the cathode conductivities of 1/2 and 2 times the reference value have also been obtained and show a similar trend. The benefit of the cathode layer thickness optimization is shown by comparing the outputs of the optimized cell and the cell with a 50 μm cathode layer, keeping the other conditions equal. As shown in Fig. 14, the cathode thickness for the maximal current output is usually around 150 μm or more. The optimization of the cathode layer thickness benefits the large pitch width design more than the small pitch width design. The optimal cathode layer thickness is larger for larger pitch width. The biggest factor influencing the optimal cathode thickness seems to be the pitch width, and not the cathode conductivity. However, the cathode layer thickness should generally be less than 300 μm even for large pitch width as there is basically no gain in the output current density by using thicker cathode layer.

The current results of the cathode layer thickness optimization are only primary. More systematic examination of various influencing factors combined with the detailed architecture of the cathode (e.g., the function layer and the current collection layer and their microstructures) will be required.

4. Summary

A 2D numerical model coupling the gas transport in porous media and electrical conduction process is presented and detailed discussions about the effects of the interconnect rib on the performance of the planar SOFC stack cell are given. The interconnect rib affects the stack cell performance mainly through the intrinsic

ohmic polarization due to the rib surface contact resistance, the increased cathode concentration polarization due to oxygen depletion in the area underneath the rib and the increased cathode ohmic polarization due to unfavorable current distribution. The interconnect rib may drastically affect the stack cell performance and the rib design optimization is of high engineering importance.

Systematic optimization of the rib size for the maximum stack cell output and sensitivity analysis on the optimization results have been carried out. The optimal rib width is found to be dependent linearly on the pitch width. The smaller the pitch width, the higher the optimal stack output, and it is recommended to use the smallest possible pitch width allowed by the engineering considerations. The parameters in the linear relationship between the optimal rib width and the pitch width are dependent on the area specific contact resistance of the rib, but are practically independent of the electrode porosity, layer thickness and conductivity. The parameters are only weakly dependent on the hydrogen molar fraction in the fuel and the results for medium hydrogen concentration are satisfactorily representative. The simple linear relationship between the optimal rib width and the pitch width and the parameters given for a range of practical contact resistance provide an easy to use guidance for the broad SOFC engineering community.

Primary results on the effects of the cathode layer thickness on the SOFC stack performance are also presented. The optimization of the cathode layer thickness is particularly beneficial for large pitch width and/or low conductivity cathode materials. The optimal cathode layer thickness is generally in the range of 100–400 μm. The larger the pitch width, the thicker the cathode layer should be.

Acknowledgements

We gratefully acknowledge the financial support of the Knowledge Innovation Program and the Key Program of the Chinese Academy of Sciences (KJCX1.YW.07), the National High-tech R&D Program of China (2007AA05Z156) and the National Science Foundation of China (10574114).

References

[1] A.V. Virkar, J. Chen, C.W. Tanner, J.W. Kim, Solid State Ionics 131 (2000) 189.
[2] J.W. Kim, A.V. Virkar, K.Z. Fung, K. Mehta, S.C. Singhal, J. Electrochem. Soc. 146 (1999) 69.
[3] S. de Souza, S.J. Visco, L.C. De Jonghe, J. Electrochem. Soc. 144 (1997) L35.
[4] R.J. Kee, P. Korada, K. Walters, M. Pavol, J. Power Sources 109 (2002) 148.
[5] M.A. Khaleel, K.P. Recknagle, Z. Lin, J.E. Deibler, L.A. Chick, J.W. Stevenson, in: H. Yokokawa, S.C. Singhal (Eds.), The Electrochemical Society Proceedings Series, Pennington, NJ, 2001 (PV2001-16).
[6] A. Solheim, in: S.C. Singhal, H. Iwahara (Eds.), The Electrochemical Society Proceedings Series, Pennington, NJ, 1993 (PV1993-4).
[7] T. Tsai, S.A. Barnett, Solid State Ionics 98 (1997) 191.
[8] S.D. Kim, H. Moon, S.H. Hyun, J. Moon, J. Kim, H.W. Lee, J. Power Sources 163 (2006) 392–397.
[9] F. Zhao, A.V. Virkar, J. Power Sources 141 (2005) 79–95.
[10] N.Q. Minh, Solid State Ionics 174 (2004) 271–277.
[11] S.D. Kim, J.J. Lee, H. Moon, S.H. Hyun, J. Moon, J. Kim, H.W. Lee, J. Power Sources 169 (2007) 265–270.
[12] M.A. Khaleel, Z. Lin, P. Singh, W. Surdoval, D. Collin, J. Power Sources 130 (2004) 136–148.
[13] B.W. Chung, C.N. Chervin, J.J. Haslam, A.Q. Pham, R.S. Glass, J. Electrochem. Soc. 152 (2) (2005) A265–A269.
[14] H.Y. Jung, S.-H. Choi, H. Kim, J.-W. Son, J. Kim, H.-W. Lee, J.-H. Lee, J. Power Sources 159 (2006) 478–483.
[15] D.H. Jeon, J.H. Nam, C.J. Kim, J. Electrochem. Soc. 153 (2) (2006) A406–A417.
[16] Z.G. Yang, K.S. Weil, D.M. Paxton, J.W. Stevenson, J. Electrochem. Soc. 150 (9) (2003) A1188–A1201.
[17] J.R. Ferguson, J.M. Fiard, R. Herbin, J. Power Sources 58 (1996) 109–122.
[18] Z. Lin, J.W. Stevenson, M.A. Khaleel, J. Power Sources 117 (2003) 92–97.
[19] Y. Ji, K. Yuan, J.N. Chung, Y.C. Chen, J. Power Sources 161 (2006) 380–391.
[20] I. Antepara, I. Villarreal, L.M. Rodríguez-Martínez, N. Lecanda, U. Castro, A. Laresgoiti, J. Power Sources 151 (2005) 103–107.
[21] J.W. Fergus, Mater. Sci. Eng. A 397 (2005) 271–283.
[22] R.B. Bird, W.E. Stewart, E.N. Lightfoot, Transport Phenomena, John Wiley & Sons, New York, 1960.
[23] E.N. Fuller, P.D. Schettler, J.C. Giddings, Ind. Eng. Chem. 58 (1966) 19.
[24] R.P. O'Hayre, S.W. Cha, W. Colella, F.B. Prinz, Fuel Cell Fundamentals, John Wiley & Sons, 2006, pp. 144 & 153.
[25] A. Bieberle, L.P. Meier, L.J. Gauckler, J. Electrochem. Soc. 148 (6) (2001) A646–A656.
[26] R. Suwanwarangkul, E. Croiset, E. Entchev, S. Charojrochkul, M.D. Pritzker, M.W. Fowler, P.L. Douglas, S. Chewathanakup, H. Mahaudom, J. Power Sources 161 (2006) 308–322.
[27] P. Aguiar, C.S. Adjiman, N.P. Brandon, J. Power Sources 138 (2004) 120–136.
[28] S.P. Jiang, Y. Ramprakash, Solid State Ionics 116 (1999) 145.
[29] A. Sawata, K. Tsuneyoshi, J. Mizusaki, H. Tagawa, Solid State Ionics 40/41 (1990) 415.
[30] S. Nagata, A. Momma, T. Kato, Y. Kasuga, J. Power Sources 101 (2001) 60.
[31] J. Yuan, M. Rokni, B. Sundén, Int. J. Heat Mass Transfer 46 (2003) 809–821.
[32] R.H. Perry, D. Green, Perry's Chemical Engineering Handbook, 7th edition, McGraw-Hill, 1997.
[33] Y. Wang, F. Yoshiba, T. Watanabe, S. Weng, J. Power Sources 170 (2007) 101–110.
[34] N.F. Bessette II, W.J. Wepfer, J. Electrochem. Soc. 142 (11) (1995) 3792–3800.
[35] COMSOL AB., COMSOL MULTIPHYSICS® Version 3.4 User's Guide, 2007.
[36] P. Deuflhard, Numer. Math. 22 (1974) 289–315.